

# Nanoscale Oxide Formation at $\alpha$ -Al<sub>2</sub>O<sub>3</sub>–Nb Interfaces

Michael K. Eusterholz,\* Torben Boll,\* Vincent Ott, Michael Stüber, Yemao Lu, Julian Gebauer, Sven Ulrich, Alexander Kauffmann, and Martin Heilmaier

Parts for metallurgical applications made from refractory metal–ceramic composites offer improved thermal shock resistance due to their capability for resistive heating compared to ones made solely from ceramics such as Al<sub>2</sub>O<sub>3</sub>. The combination of Al<sub>2</sub>O<sub>3</sub> and Nb is intriguing as both show similar thermal expansion behavior over a wide temperature range. The high affinity of Nb for O to form nonprotective oxides, however, hampers its use in oxidative environments. Formation of such phases at the ceramic–metal interface can have detrimental effects on the cohesion of the composites. For this work, nanocrystalline Nb films are deposited on sapphire substrates by magnetron sputtering to study diffusion of O and high-temperature phase formation at a refractory metal–ceramic interface during heat treatment under Ar at 1600 °C. A combined approach of atom probe tomography and transmission electron microscopy for compositional and crystallographic analyses reveals that at triple junctions of the sapphire–Nb interface with Nb grain boundaries, heterogeneous nucleation of nanoscale NbO<sub>2</sub> occurs, which further reacts with Al<sub>2</sub>O<sub>3</sub> to form AlNbO<sub>4</sub>, while the Nb film itself remains metallic. Fast O transport through grain boundaries leads to internal oxidation at the interface, whereas regions further away from Nb grain boundaries remain unchanged.

The development of composites based on refractory ceramics and refractory metals (RM),<sup>[1–5]</sup> thus, aims at taking advantage of the benefits of ceramics, but also at exploiting the ductility and electrical conductivity of the RM.<sup>[5–8]</sup> The electrical conductivity offers a path to strongly reduce the thermal gradients through resistive heating of the parts before service. Among ceramics and metals, the combination of body-centered-cubic Nb (Nb<sub>bcc</sub>) and (hexagonal)  $\alpha$ -Al<sub>2</sub>O<sub>3</sub> is particularly promising due to their similar thermal expansion behavior ( $\alpha_{\text{Nb}} = 8.0$  to  $10.3 \times 10^{-6} \text{ K}^{-1[9]}$  and  $\alpha_{\text{Al}_2\text{O}_3} = 9.3$  to  $11.2 \times 10^{-6} \text{ K}^{-1[10]}$  from 527 to 1827 °C) and, thus, low-thermal misfit stresses during fabrication and service.


A novel approach in the field is the development of coarse-grained (particle sizes of up to a few mm) ceramic–metal composites<sup>[6,11–13]</sup> to improve creep and thermal shock resistance compared to fine-grained composites. Heat treatments during manufacturing such as sintering can cause reactions of the involved phases

with each other or with the environment, which will inevitably affect the properties of the composite. Weidner et al.<sup>[14]</sup> reported on refractory binary and possibly ternary metal oxide formation in Nb–Al<sub>2</sub>O<sub>3</sub> and Ta–Al<sub>2</sub>O<sub>3</sub> composites prepared by Zienert et al.<sup>[6]</sup> by sintering under Ar. In our previous work,<sup>[15]</sup> we advanced the understanding of the formation of refractory oxides with a joint approach of experimental methods and thermodynamic calculations. We linked the formation of the binary oxide NbO to the decreasing O solubility in Nb during cooling in the furnace. Besides the well-known embrittlement of bcc metals by

## 1. Introduction

Components for high-temperature applications like furnace linings in melt-casting processes require materials designed for operating temperatures of around 1500 °C and beyond. Conventionally applied materials are engineering ceramics, which are chosen based on their excellent creep, corrosion, and erosion resistance. However, the large temperature gradients cause ceramic-based parts to suffer failure by intense thermal shock when in contact with metallic liquids.

M. K. Eusterholz, T. Boll, A. Kauffmann, M. Heilmaier  
Institute for Applied Materials – Materials Science and Engineering (IAM-WK)  
Karlsruhe Institute of Technology (KIT)  
Engelbert-Arnold-Str. 4, 76131 Karlsruhe, Germany  
E-mail: michael.eusterholz@kit.edu; torben.boll@kit.edu

 The ORCID identification number(s) for the author(s) of this article can be found under <https://doi.org/10.1002/adem.202201441>.

© 2023 The Authors. Advanced Engineering Materials published by Wiley-VCH GmbH. This is an open access article under the terms of the Creative Commons Attribution-NonCommercial-NoDerivs License, which permits use and distribution in any medium, provided the original work is properly cited, the use is non-commercial and no modifications or adaptations are made.

DOI: 10.1002/adem.202201441

T. Boll, Y. Lu  
Institute of Nanotechnology (INT)  
Karlsruhe Institute of Technology (KIT)  
Hermann-von-Helmholtz-Platz 1, 76344 Eggenstein-Leopoldshafen, Germany

T. Boll  
Karlsruhe Nano Micro Facility (KNMFI)  
Karlsruhe Institute of Technology (KIT)  
Hermann-von-Helmholtz-Platz 1, 76344 Eggenstein-Leopoldshafen, Germany

V. Ott, M. Stüber, J. Gebauer, S. Ulrich  
Institute for Applied Materials – Applied Materials Physics (IAM-AWP)  
Karlsruhe Institute of Technology (KIT)  
Hermann-von-Helmholtz-Platz 1, 76344 Eggenstein-Leopoldshafen, Germany

already low levels of interstitial solutes,<sup>[16,17]</sup> the local oxidation of Nb and the resulting lattice strain due to changing volumes will introduce additional interfaces and lower the strength of the material.<sup>[18]</sup> Indeed, Günay et al.<sup>[7]</sup> investigated room- and high-temperature compression behavior of Nb–Al<sub>2</sub>O<sub>3</sub> composites and observed crack initiation at regions where NbO formed. Besides these consequences for the mechanical behavior, protecting the metallic component of the composite from oxidation also infers sufficient electrical conductivity for the resistive heating of the parts.

To selectively study the effects of O contamination on a ceramic–metal interface regardless of powder quality and processing conditions, we prepared high-purity film composites by magnetron sputtering of Nb on <0001>-oriented single-crystalline corundum (Al<sub>2</sub>O<sub>3</sub>) substrates. A subsequent heat treatment at 1600 °C simulates the conditions of a conventional sintering procedure for castables. To identify forming phases and the role of Nb grain boundaries on the chemistry at the Nb–Al<sub>2</sub>O<sub>3</sub> interface, the high-resolution techniques atom probe tomography (APT) and transmission electron microscopy (TEM) along with energy-dispersive X-ray spectroscopy (TEM–EDX) are used for compositional, imaging, and diffraction analysis. While APT offers 3D chemical analysis with high accuracy,<sup>[19–22]</sup> TEM can verify the data with straightforward crystallographic characterization.

## 2. Results

The diffraction pattern of the as-deposited Nb film shown in **Figure 1** suggests a polycrystalline film with strong preferential orientation of Nb grains and an orientational relationship to the substrate (S) of (0001)<sub>S</sub> || (110)<sub>Nb</sub>. The obtained data is shifted by 0.1° to smaller diffraction angles, that is, lattice plane distances

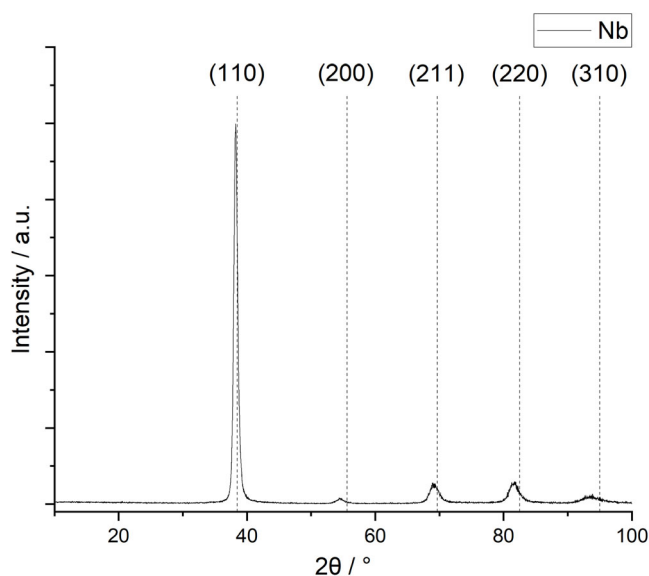


**Figure 1.** XRD pattern of the 30 μm Nb film on <0001>-oriented sapphire. The diffraction peaks of the polycrystalline Nb (space group 229) appear to be slightly shifted to smaller angles by about 0.1°, that is, greater lattice plane distances. The diffractometer was calibrated with a polycrystalline Si specimen.

greater by about 0.2% compared to Nb diffraction peak positions from literature,<sup>[23]</sup> suggesting a film growth with minor tensile lattice strain in growth direction.

**Figure 2a** depicts a high-resolution transmission electron micrograph (HRTEM) of a region including a section of the Al<sub>2</sub>O<sub>3</sub>–Nb interface in the as-deposited state. No reaction layer was detected at the interface, which is in agreement with literature reports on a similar fabrication route.<sup>[24,25]</sup> The interface does not appear atomically sharp due to roughness of the substrate of a few atomic layers. The Nb film (on the right in **Figure 2**) consists of grains of about 10–20 nm in size normal to the growth direction and a high defect density, including misfit dislocations and small-angle grain boundaries, which are highlighted in **Figure 2b**. Local fast-Fourier transforms (FFTs) show the strong orientation preference for Al<sub>2</sub>O<sub>3</sub> described above with {0001}<sub>S</sub> || {110}<sub>Nb</sub>. The d spacing of the (110) plane of Nb in

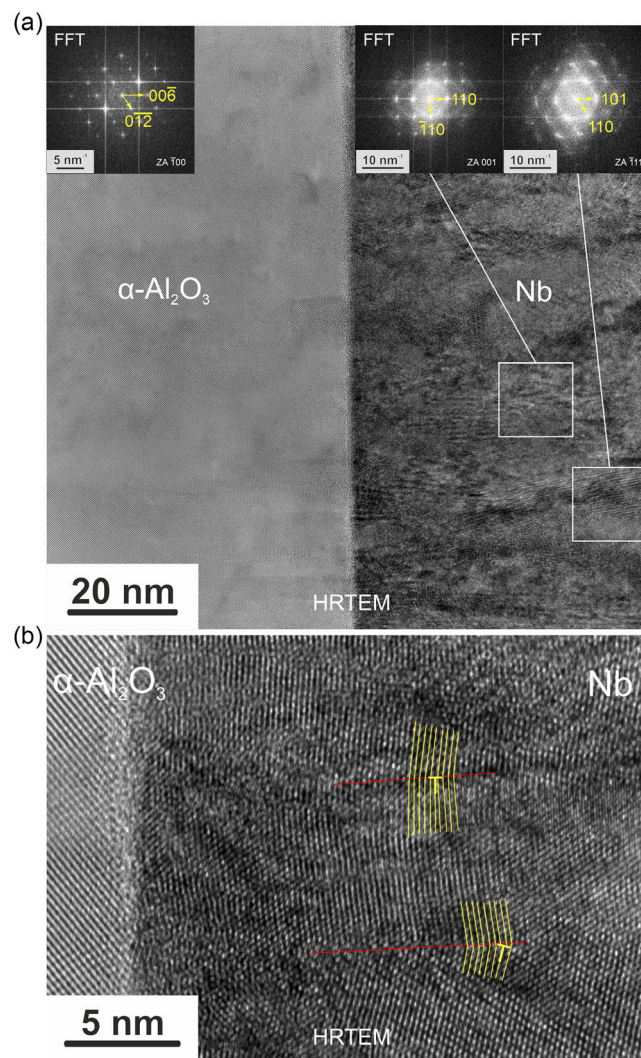


**Figure 2.** a) High-resolution TEM image of α-Al<sub>2</sub>O<sub>3</sub>–Nb<sub>bcc</sub> interface region and FFT taken from both phases (as-deposited state). b) Magnified HRTEM section of the interface depicted in (a). Grain boundaries (red) and lattice planes with extra half-planes (yellow) are shown as examples for lattice defects in the Nb film.

the FFT in Figure 2a is 2.3 Å. With a d spacing of the Al<sub>2</sub>O<sub>3</sub> ( $\bar{1}20$ ) plane of 2.38 Å,<sup>[26]</sup> the lattice misfit is 3.4%, not considering the interdiffusion zone.

The reconstructed APT elemental map shown in Figure 3a contains the ceramic–metal interface with regions rich in Al+O comprising ions and Nb ions on the left and right, respectively. Commonly, planar features like interfaces are oriented perpendicular to the analysis direction z to achieve the highest possible resolution of APT.<sup>[22]</sup> Boundaries of different orientations in the APT specimen may appear broader by up to several nanometers.<sup>[27,28]</sup> However, orienting the interface parallel to the analysis direction or with a tilt angle will yield a larger interface area to investigate. In addition, it grants higher mechanical stability to the tip specimen in the electric field of APT. Poor adhesion at interfaces<sup>[19,29]</sup> and field-induced stress due to the sudden change in the evaporation field strength at an interface<sup>[19]</sup> drastically increase the chance for a tip fracture. In the present case, the interface is therefore oriented nearly parallel to the analysis direction. The compositional profile in Figure 3b was created as a proxigram of an 35 at% Nb isosurface to account for the curvature of the interface visible in the reconstructed APT tip in Figure 3a. No contaminants except <0.1 at% Ga at the interface from the preparation with focused ion beam (FIB) were found. The measured Al:O ratio in  $\alpha$ -Al<sub>2</sub>O<sub>3</sub> conforms to 45:55. This underestimation of O can be attributed to neutral evaporation, a known phenomenon<sup>[30–32]</sup> in APT for bulk metal oxides and nitrides. Apart from the overlap of O<sub>2</sub><sup>2+</sup> with O<sup>+</sup> ions in the mass spectrum which generally hampers the correct determination of the O concentration, Karahka et al.<sup>[33]</sup> suggested that metal oxide phases exhibit neutral evaporation of O, as in these compounds, metal ions are typically less strongly bound than O ions and will evaporate at lower electrical fields. O ions in the resulting O enriched layer are then likely to desorb associatively, forming O molecules that are not detected as ions.

In Nb<sub>bcc</sub>, about 0.5 at% O was found by APT, which may be an expected value for the solubility limit of Nb for O at room temperature, if extrapolated from known solubilities at higher temperatures.<sup>[34]</sup> Between the two phases  $\alpha$ -Al<sub>2</sub>O<sub>3</sub> and Nb<sub>bcc</sub>, an

interfacial region of deviating composition is present. This interlayer consists of Al, Nb, and O, with an Al content of nearly 40 at% and Nb between 10 and 25 at%. Figure 3c depicts an Al and Nb contour plot for the isoconcentration values between 10 and 25 at% Nb, that is, it offers a view of the interlayer region perpendicular to the direction of the concentration profile. This region appears to have an inhomogeneous distribution of Al and Nb with Al-rich regions of compositions corresponding to Al<sub>2</sub>O<sub>3</sub>, and Al-lean regions, confirming the presence of local roughness at the  $\alpha$ -Al<sub>2</sub>O<sub>3</sub>–Nb interface.

The annealing treatment of the sample at 1600 °C yields a local change of the interface structure (Figure 4a, high-angle annular dark-field image (HAADF) image). Generally, regions as marked with “1” show no reaction layer but maintain a compositionally sharp interface, as shown by the EDX profile (Figure 4b). However, additionally, interfacial particles can be found, possibly consisting of Al, Nb, and O, as suggested by EDX (Figure 4c). These particles were not found in the as-deposited specimen and appear to have partially grown into the sapphire substrate. Unfortunately, no unequivocal phase identification was possible with electron diffraction. Both EDX profiles yield an atomic ratio of about 50 Al–50 O at% in alumina, that is, an underestimation of O owing to the low sensitivity of EDX for this element. Although an increased O content in Nb<sub>bcc</sub> can be found, the selected-area diffraction patterns (SAD) d) and e) taken from both sides of the interface confirm only the initially present phases  $\alpha$ -Al<sub>2</sub>O<sub>3</sub> and Nb<sub>bcc</sub>, which contradict the O concentration given by EDX. A combination of scanning transmission electron microscopy (TEM) and SAD (4DSTEM, Figure 5) shows lateral Nb<sub>bcc</sub> grain growth in the vicinity of the interface, resulting in the loss of the fiber texture. The particle shown in Figure 4a appears to be located at a triple junction with a remaining Nb<sub>bcc</sub> grain boundary.

The O contour plot of a reconstructed APT tip displayed in Figure 6a shows the interface between  $\alpha$ -Al<sub>2</sub>O<sub>3</sub> (yellow) and Nb<sub>bcc</sub> (dark blue). At the interface, a region with an increased O concentration is indicated with red color, hinting at an additional phase formation. The light blue line in Nb<sub>bcc</sub> suggests the presence of a Nb<sub>bcc</sub> grain boundary enriched in O, forming a

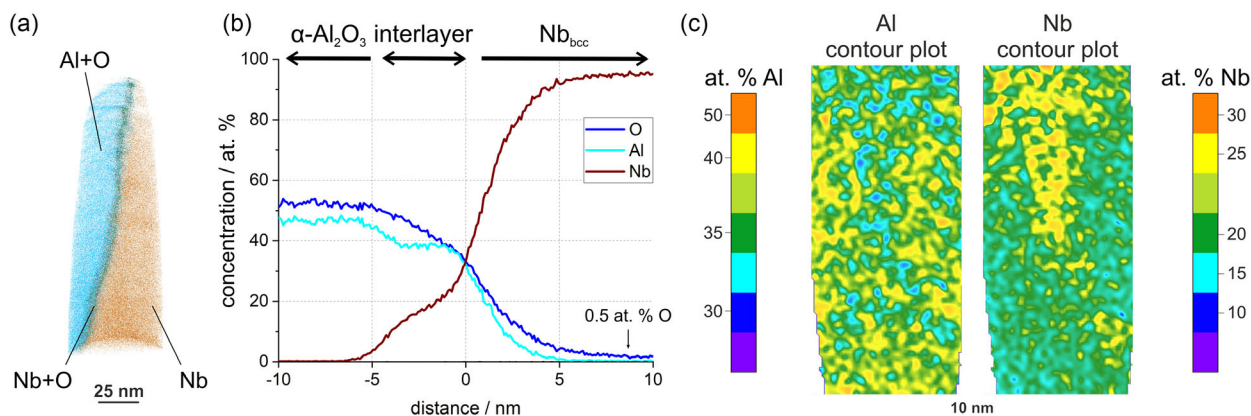


**Figure 3.** a) Reconstructed APT elemental map of the as-deposited specimen tip including the interface. The colors display regions rich in the indicated elements. b) APT proxigram through the interface in (a) for a 35 at% Nb isosurface. c) Al and Nb contour plots of the projection into a plane parallel to the tip axis (z,x plane), depicting the interlayer region perpendicular to the concentration profile direction in (b) between 10 and 25 at% Nb.

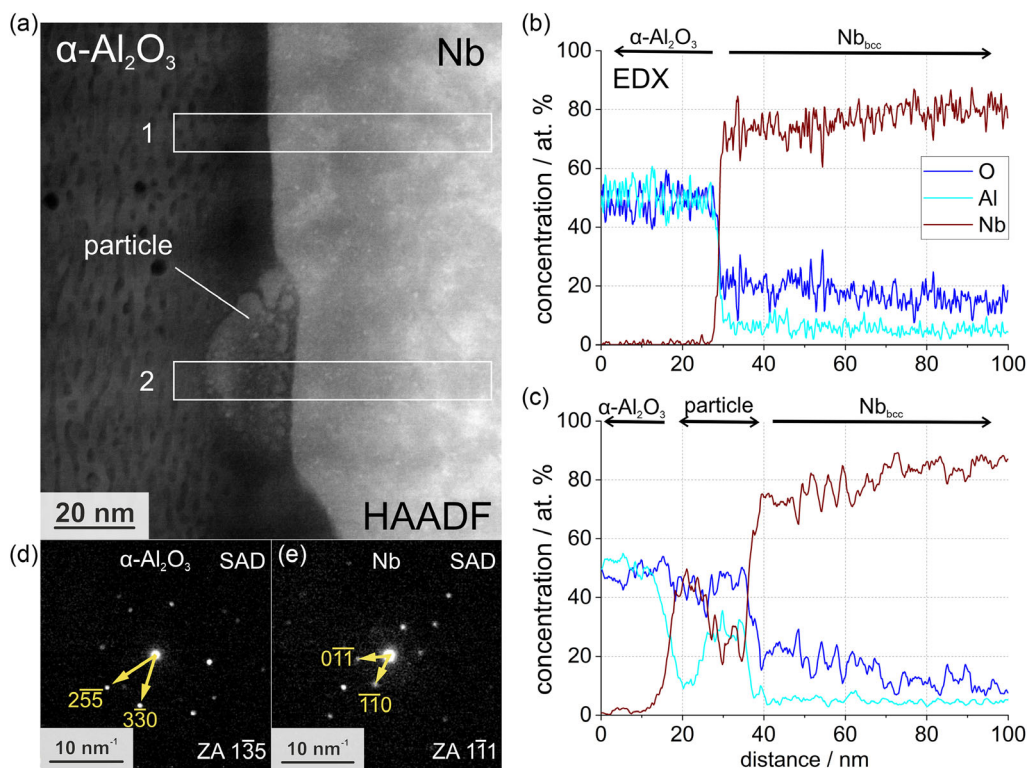


**Figure 4.** a) HAADF image showing the presence of a single particle at the  $\alpha\text{-Al}_2\text{O}_3\text{-Nb}_{\text{bcc}}$  interface (annealed state). b) TEM-EDX profile across the interface in a region without particles, marked as white box (1) in (a). c) TEM-EDX profile across the particle (white box 2) in (a). d, e) SADs for the phases  $\alpha\text{-Al}_2\text{O}_3$  (space group 167) and  $\text{Nb}_{\text{bcc}}$  (space group 229).

triple junction with the  $\alpha\text{-Al}_2\text{O}_3\text{-Nb}_{\text{bcc}}$  interface, that is, a situation as depicted in Figure 4 and 5. The Gibbs interfacial excess of  $\text{O}^{[35]}$  at the Nb grain boundary amounts to about 16 atoms  $\text{nm}^{-2}$ . Considering a Nb (001) plane with  $a_{\text{Nb}} = 3.3 \text{ \AA}$ ,<sup>[36,37]</sup> nine lattice sites are available for an area of  $1 \text{ nm}^2$  and the calculated excess value would correspond to nearly two atomic planes, that is, suggesting that a thin oxide phase may have formed in the vicinity of the grain boundary. Figure 6c shows the Al (left) and Nb (right) concentration maps of a vertical cross section across the ceramic-metal interface in the region marked with a black cuboid in the Al contour plot in Figure 6b. Between  $\alpha\text{-Al}_2\text{O}_3$  and  $\text{Nb}_{\text{bcc}}$ , two regions can be distinguished. Depicted in light green in the Nb concentration map, a layer with a composition of about 30 at% Nb and 60 at% O appears to be interspersed with Al-rich regions with an Al:Nb:O ratio of about 1:1:4. This hints at nucleation of a ternary phase ( $\text{AlNbO}_4$ ) in the interfacial region, which seems to be less prevalent in the top part of the section. Figure 6d depicts a compositional profile between  $\alpha\text{-Al}_2\text{O}_3$  and  $\text{Nb}_{\text{bcc}}$  across the latter region marked with the red cylinder in Figure 6c. The Al:O ratio in  $\text{Al}_2\text{O}_3$  is about 45:50. The O deficiency can be explained, as for Figure 3b, by neutral evaporation in bulk metal oxides and should also be taken into account for the interfacial region. Considering the slight underestimation of the O content, the composition of the interfacial region corresponds to  $\text{NbO}_2$  and has a width of several nanometers. In contrast to Figure 3b, where the broad O gradient indicates a lower accuracy of APT, a significant overestimation of

the width can be ruled out. As the origin of neutral evaporation of O described above does not apply to metals, APT offers more reliability for the O content in  $\text{Nb}_{\text{bcc}}$  and confirms an increased O amount of about 10 at% in the metal surrounding the grain boundary. Figure 6e shows a concentration profile through the  $\text{Al}_2\text{O}_3\text{-Nb}$  interface in a region unaffected by  $\text{Nb}_{\text{bcc}}$  grain boundaries. Compared to the as-received state in Figure 3b, the interface remains chemically unchanged, with a slight increase of the O concentration in  $\text{Nb}_{\text{bcc}}$  to about 1 at%.

The results displayed in Figure 6 suggest the formation of  $\text{NbO}_2$  in the vicinity of an O-enriched  $\text{Nb}_{\text{bcc}}$  grain boundary and the beginning nucleation and growth of  $\text{AlNbO}_4$  between  $\alpha\text{-Al}_2\text{O}_3$  and  $\text{NbO}_2$ . However, further APT measurements show that the  $\text{Nb}_{\text{bcc}}$  grain boundaries in regions closer to the outer surface of the Nb film are more enriched with O compared to those near the substrate. Figure 7a depicts an O concentration map of an APT specimen taken from  $\text{Nb}_{\text{bcc}}$  region about  $20 \mu\text{m}$  away from the substrate.  $\text{Nb}_{\text{bcc}}$  grains indicated in purple (about 1 at% O) are separated by grain boundaries highly enriched with O, as shown by the concentration profile in Figure 7b created along the black arrow in Figure 7a. The decoration of up to 50 at% O amounts to a Gibbsian excess of  $65 \text{ atoms nm}^{-2}$ , which corresponds to about 14 atomic layers if local formation of  $\text{NbO}$  is assumed. The O concentration is, thus, significantly higher than for the grain boundary depicted in Figure 6a (locally up to 30 at% O, Gibbsian excess of  $6 \text{ atoms nm}^{-2}$ ). The formation of  $\text{NbO}_2$  in the vicinity of the latter can, thus, not be explained with O solely

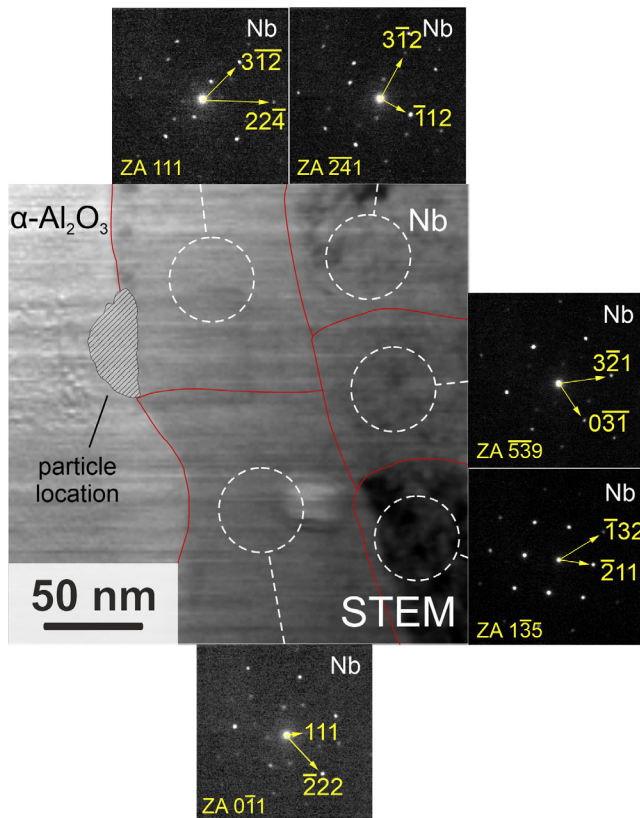


**Figure 5.** Scanning transmission electron micrograph and  $\text{Nb}_{\text{bcc}}$  SAD patterns in the vicinity of the region depicted in Figure 4.  $\text{Nb}_{\text{bcc}}$  grain boundaries are indicated by red lines. For better visibility, the hatched region highlights the location of the particle shown in Figure 4.

supplied by the grain boundary, that is, stemming from the atmosphere. Indeed, even in a distance of about 10 nm from the oxide interlayer, small amounts of Al (about 0.5 at%) can be found in  $\text{Nb}_{\text{bcc}}$  in the dataset underlying Figure 6, indicating that simultaneous dissolution of Al and O from the sapphire substrate can be accountable for additional O to form  $\text{NbO}_2$ .

### 3. Discussion

The sapphire–Nb film composites were prepared by magnetron sputtering at room temperature, that is, a low homologous temperature of about 0.15 (ratio of the substrate temperature and the melting temperature of Nb). Following the Thornton structure-zone model,<sup>[38]</sup> the limited mobility of Nb atoms at the selected deposition conditions leads to nucleation and columnar growth of Nb grains of only 10–20 nm in width, creating an extended network of grain boundaries in the Nb film. The sapphire lattice can be described by a rhombohedral unit cell<sup>[39,40]</sup> and for the preferred orientation of Nb according to  $(0001)_{\text{S}} \parallel (110)_{\text{Nb}}$  the Nb film can be regarded as locally heteroepitaxial to the substrate. The crystallographic relationship observed in this work differs from the previous works of Rühle et al., who studied various metal–ceramic interfaces and, among these, interfaces between

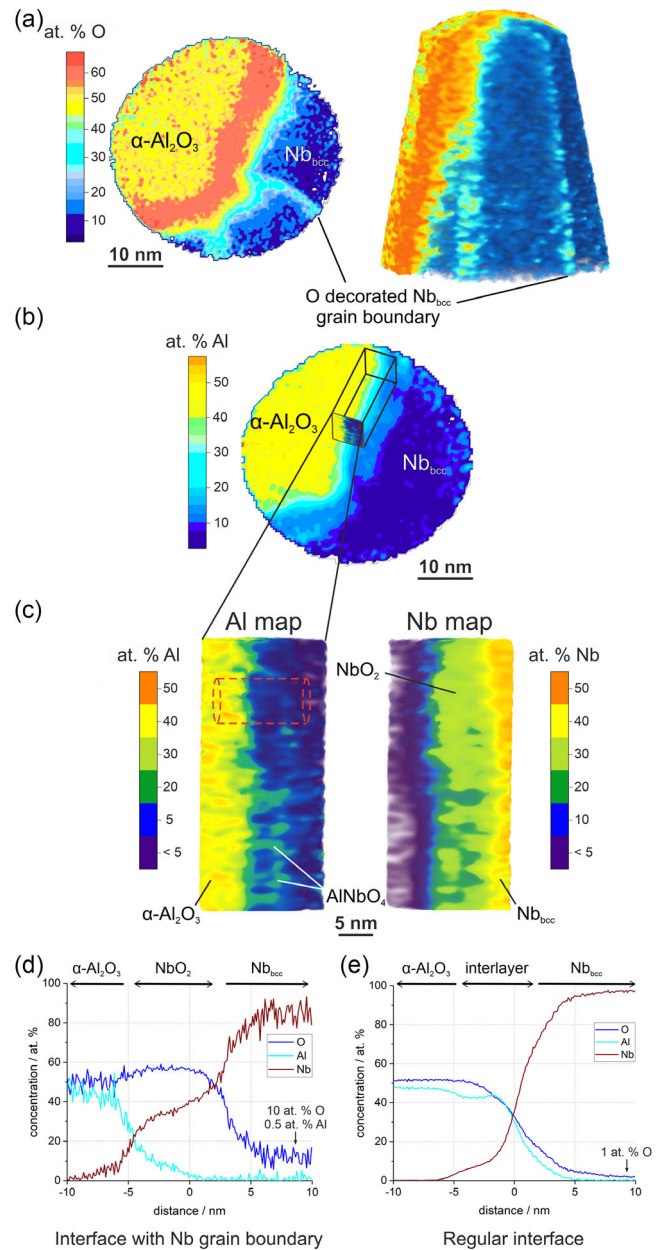


**Figure 6.** a) O contour plot of the projection of a reconstructed APT tip into a plane parallel to the tip axis ( $z,x$  plane). The plot contains a triple junction of the  $\alpha\text{-Al}_2\text{O}_3\text{-Nb}_{\text{bcc}}$  interface with a  $\text{Nb}_{\text{bcc}}$  grain boundary. b) Corresponding Al contour plot. c) Al (left) and Nb (right) concentration maps of a vertical cross section taken from the region marked with a black cuboid in (b). d) Compositional profile (Nb isovalue 40 at%) across the Al-lean region marked with a red cylinder. e) Compositional profile (Nb isovalue 37 at%) across the  $\text{Al}_2\text{O}_3\text{-Nb}$  interface in a region unaffected by  $\text{Nb}_{\text{bcc}}$  grain boundary.

Nb and sapphire.<sup>[41–45]</sup> Mayer et al.<sup>[43,46]</sup> showed that the interface  $(0001)_{\text{S}} \parallel (111)_{\text{Nb}}$  is semicoherent for the investigated film thickness of 100 nm and comprises coherent regions alternating with misfit dislocations to accommodate the lattice mismatch. However,  $\alpha\text{-Al}_2\text{O}_3$  precipitates forming in Nb matrix during internal oxidation of Nb–Al alloys appear to have an orientation

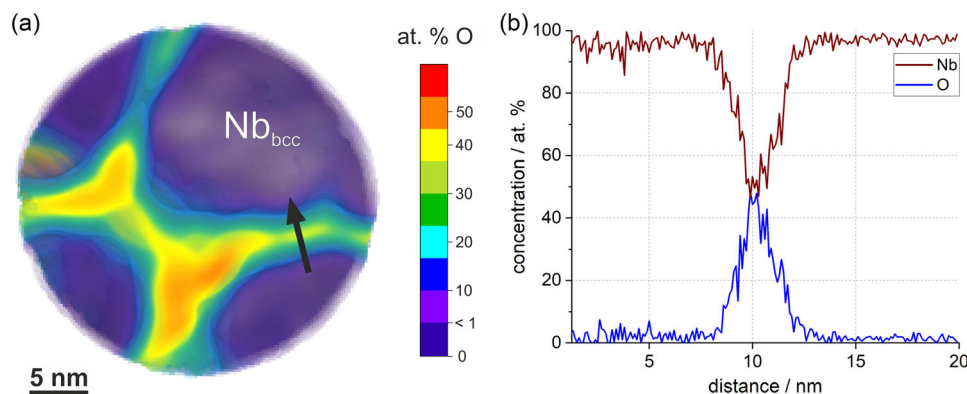


**Figure 7.** a) O concentration map in a Nb<sub>bcc</sub> region 10 μm from the outer surface, that is, 20 μm away from the substrate. b) Concentration profile through a grain boundary along the black arrow in (a).

relationship of the terminating interface planes of (0001)<sub>S</sub> || (110)<sub>Nb</sub>,<sup>[24]</sup> as in the present work. According to Gutekunst et al.,<sup>[44]</sup> the discrepancy between the orientation relationships is due to kinetic differences during the growth process. Mader<sup>[24]</sup> attributed this orientation relationship to the good match of the (11̄0) Nb planes with the prismatic planes (2̄1̄1̄0) of Al<sub>2</sub>O<sub>3</sub> along [11̄0] Nb. Additionally, different from other orientation relationships, the distance between the O atoms along the [011̄0] close-packed direction of Al<sub>2</sub>O<sub>3</sub> appears to be closely related to the distance between the Nb atoms along [001] for the (0001)<sub>S</sub> || (110)<sub>Nb</sub> relationship. Thus, according to Mader,<sup>[24]</sup> the configuration present in this work is of lower energy than other Al<sub>2</sub>O<sub>3</sub>–Nb interfaces.<sup>[24,25]</sup>

The peculiar interlayer found in the APT profile in Figure 3b can be explained by lattice distortions at the interface and the observed interface roughness in Figure 2b. The changing slopes in the Al and Nb signals seem to indicate a substitution of Al by Nb; however, Al<sub>2</sub>O<sub>3</sub> is a stoichiometric phase and its bulk solubility for Nb is negligible.<sup>[44,47,48]</sup> As the deposition is carried out at relatively mild conditions (magnetron sputtering, room temperature, no additional bias, that is, the arriving Nb atoms have kinetic energies in the range of a few eV), implantation of Nb atoms into the substrate is not relevant. The formation of a ternary phase is unlikely in the present case, as in the Al–Nb–O system; according to thermodynamic calculations, ternary phases only exist in the Al<sub>2</sub>O<sub>3</sub>–Nb<sub>2</sub>O<sub>5</sub> quasibinary section or if NbO<sub>2</sub> is present with additional O available.<sup>[15,47]</sup> The formation of such a phase, thus, first requires the oxidation of Nb to at least NbO<sub>2</sub>, that is, a substantial amount of available O.<sup>[15]</sup> Instead, no particular O incorporation into Nb<sub>bcc</sub> near the interface is found (<1 at%). The slight apparent roughness of the interface in Figure 2b and the neighboring Al-rich and Al-lean regions in Figure 3c rather suggest that the apparent composition of the interlayer originates from local roughness and the lateral proximity of α-Al<sub>2</sub>O<sub>3</sub> and Nb<sub>bcc</sub> regions. Due to the aforementioned lower accuracy<sup>[22]</sup> perpendicular to the analysis direction, that is, in the x–y plane, the width of the interlayer region is overestimated, as can be deduced from the width of the O concentration gradient. The interlayer rather extends only over a range of 1 nm or less.

The subsequent thermal treatment at 1600 °C was expected to increase the O concentration in the vicinity of the interface due to the accelerated transport of O from other possible sources, for example, entrapped O inside the crucible or surface contaminations on the sample. The above-mentioned low O<sub>2</sub> partial pressure does not consider additional O which may stem from contaminations of the crucible and sample surface or CO formed by the reaction of O impurities in Ar with the graphite-lined chamber. For equilibrium conditions, with sufficient O supply, a reaction sequence according to Nb<sub>bcc</sub> → NbO → NbO<sub>2</sub> → Nb<sub>2</sub>O<sub>5</sub> and subsequently, with the presence of Al<sub>2</sub>O<sub>3</sub>, formation of Al niobate compounds (AlNb<sub>49</sub>O<sub>124</sub>, AlNb<sub>11</sub>O<sub>29</sub>, AlNbO<sub>4</sub>) is expected.<sup>[34,47,48]</sup> As mentioned above, the formation of AlNbO<sub>4</sub> is possible through a reaction of Al<sub>2</sub>O<sub>3</sub>, NbO<sub>2</sub>, and additional O.<sup>[15]</sup> Our previous combined approach<sup>[15]</sup> of experimental investigations and thermodynamic calculations showed that sintering of Al<sub>2</sub>O<sub>3</sub>–Nb refractory composites involving additional O (up to 50 at%) from external sources like the atmosphere or binder additions would, on a scale observable with SEM methods, only form NbO once the solubility limit of O in Nb<sub>bcc</sub> is exceeded. Both, the EDX data in Figure 4c and the APT data in Figure 6e suggest an O content in Nb<sub>bcc</sub> too low for an oxide formation within Nb<sub>bcc</sub>. Figure 4e instead proves the surrounding region to remain in the form of Nb<sub>bcc</sub>, although the expansion of the lattice spacing suggests a considerable enrichment with O. The SAD also indicates that the Al<sub>2</sub>O<sub>3</sub>–Nb orientation relationship is maintained but the 4DSTEM data in Figure 5 shows that grain growth occurred in the Nb film to grain sizes above 100 nm, thereby reducing the lattice defect density and internal surface area available for O transport. However, remaining defects like misfit dislocations and grain boundaries act as O sinks and account for locally increased O content and can also explain the increased O concentration in Nb<sub>bcc</sub> found with EDX in Figure 4b,c. Such an O-enriched Nb<sub>bcc</sub> grain boundary is shown in Figure 6a, forming a triple junction with the highly O-enriched Al<sub>2</sub>O<sub>3</sub>–Nb interface, at which an additional oxide appears to have formed (red). The O-decorated grain boundary suggests diffusion of O from outside the specimen, which cannot stem from a reaction with the sapphire substrate, as a reduction of Al<sub>2</sub>O<sub>3</sub> ( $\Delta G_{1873\text{ K}} = -718\text{ kJ mol}^{-1}$ ) in the sole presence of Nb<sub>bcc</sub> to form any Nb oxide ( $\Delta G_{1873\text{ K}} = -504\text{ kJ mol}^{-1}$ ) is

thermodynamically unfavorable.<sup>[49,50]</sup> However, comparison of the findings in Figure 6 and 7 suggests that O transport through grain boundaries alone cannot lead to nucleation of the found NbO<sub>2</sub>. As at highly O-enriched Nb<sub>bcc</sub> grain boundaries away from the substrate only NbO forms (Figure 7), further oxidation to NbO<sub>2</sub>, despite a lower O concentration at the grain boundary (Figure 6), requires a reaction with O from the adjacent sapphire substrate. The presence of Al in Nb<sub>bcc</sub> in the vicinity hints at a dissolution of Al<sub>2</sub>O<sub>3</sub> in the metal, which may, together with additional O supplied by the grain boundary, ultimately result in the formation and growth of AlNbO<sub>4</sub> as interfacial oxide. The found Al-containing regions in the vertical cross section in Figure 6c have a concentration matching this niobate compound and support this claim. With this information, the EDX profile in Figure 4c could also be interpreted as containing AlNbO<sub>4</sub>. The particle depicted could be taken as a region that evolved from a situation captured in Figure 6. Ternary compound formation, thus, appears to be possible without sufficient O to form Nb<sub>2</sub>O<sub>5</sub>.

Regarding regions at the Al<sub>2</sub>O<sub>3</sub>–Nb interface further away from Nb<sub>bcc</sub> grain boundaries, Figure 4b and 6e disclose that such regions still show a compositionally sharp interface. The O concentration in Nb<sub>bcc</sub> of about 1 at% in Figure 6e is certainly more reliable than the value obtained with EDX and matches the conception that the Nb layer remains metallic. The 10 at% O found with APT in Nb<sub>bcc</sub> at the triple junction in Figure 6d could stem from both, the Nb<sub>bcc</sub> grain boundary and dissolution of Al<sub>2</sub>O<sub>3</sub> in Nb<sub>bcc</sub>, but exceeds the solubility limit of the solid solution even for the annealing temperature of 1600 °C (being only nearly 6 at%).<sup>[51]</sup> Local precipitation of NbO can be a reasonable explanation, but as APT data analysis did not provide any evidence for the formation of O-rich clusters, we can assume that a thermodynamically stable state was not yet reached. Already initiated Nb oxide nucleation is likely, but without sufficient growth of nuclei to verify their existence. A longer exposure to O would eventually yield nucleation and growth of NbO in the Nb<sub>bcc</sub> matrix. NbO crystallizes in a simple cubic structure (similar to NaCl, space group 221) and a lattice parameter of 4.21 Å.<sup>[52]</sup> Its formation in a refractory ceramic–metal composite designed to have electrical conductivity is not unfavorable in the view of electrical conductivity as it is considered metallic.<sup>[53,54]</sup> However, the lattice parameter difference to Nb<sub>bcc</sub> ( $a = 3.3$  Å) and the lower coefficient of thermal expansion  $\alpha$  (about  $6.5 \times 10^{-6} \text{ K}^{-1}$  between 247 and 850 °C)<sup>[55]</sup> will induce substantial lattice strain. The binary Nb oxide shown in Figure 6 was determined as NbO<sub>2</sub>. At room temperature, the crystal structure of this compound is described as a distorted tetragonal superstructure with a rutile-type sublattice and  $a = 13.695$  Å and  $c = 5.981$  Å (space group 88).<sup>[56,57]</sup> Around 800 °C, NbO<sub>2</sub> undergoes a reversible second-order phase transition into a rutile lattice.<sup>[56–59]</sup> As the high-temperature modification shows metallic conductivity ( $\approx 10^3 \text{ S cm}^{-1}$ ),<sup>[59]</sup> NbO<sub>2</sub> formation may also not be electrically detrimental. It will, however, result in significant lattice strain and, especially during thermal cycling due to its strongly anisotropic thermal expansion ( $\alpha_a = 3.3 \times 10^{-6} \text{ K}^{-1}$  and  $\alpha_c = 18.8 \times 10^{-6} \text{ K}^{-1}$  at 900 °C),<sup>[60]</sup> mechanically weaken the ceramic–metal interface. Figure 6c shows that, for the present condition, AlNbO<sub>4</sub> will begin to form at the interface. This monoclinic compound (space group 12) is currently investigated as a material for thermal barrier coatings due to its low thermal conductivity.<sup>[61]</sup> But it is reported to have poor

protection against oxidation<sup>[62,63]</sup> and an anisotropic thermal expansion behavior,<sup>[64]</sup> although not as severe as NbO<sub>2</sub>. For a thermal shock-resistant and heat-conducting composite, its formation can be assessed as detrimental. If Nb transforms to Nb<sub>2</sub>O<sub>5</sub>, the thermodynamically stable state of the Nb–O system,<sup>[54]</sup> the electrical conductivity will entirely be lost.<sup>[65]</sup> Mechanically, the formation of Nb<sub>2</sub>O<sub>5</sub> is also unfavorable, as its very low and anisotropic thermal expansion coefficient<sup>[66]</sup> and the large difference in molar volume compared to Nb metal are known to cause severe spallation.<sup>[18]</sup>

A future approach to assess the role of interfacial oxide formation for the mechanical properties is possible by comparison with powder-based refractory composites. The investigation of interfaces between Al<sub>2</sub>O<sub>3</sub>, Nb, and Nb oxides regarding crack initiation sites will shed more light on the effect of oxide formation on interface cohesion. For both, manufacturing and service of components based on Al<sub>2</sub>O<sub>3</sub>–Nb composites, suppression of O grain boundary diffusion in Nb is vital to avoid fast oxidation at the ceramic–metal interface. The approach to develop coarse-grained Al<sub>2</sub>O<sub>3</sub>–Nb refractory composites, therefore, does not only offer improved creep and thermal shock resistance compared to fine-grained composites but reduces available pathways for internal oxidation.

## 4. Conclusion

High-purity film composites prepared by magnetron sputtering prove to be suitable model systems to study high-temperature phase formation at refractory metal–ceramic interfaces. Although the techniques APT and TEM–EDX suffer from an under- or over-estimation of O, the complementary approach helps to avoid misinterpretations of compositional analysis data. Deposition of the metal film at low homologous temperatures inevitably yields a small grain size at this temperature, rendering the specimen very suitable to study grain boundary diffusion of O to the ceramic–metal interface from outside the specimen. While the bulk Nb itself remains metallic, the accelerated grain boundary diffusion of O compared to sole bulk diffusion leads to nucleation of NbO along grain boundaries in Nb<sub>bcc</sub> and NbO<sub>2</sub> at the Al<sub>2</sub>O<sub>3</sub>–Nb interface. NbO<sub>2</sub> appears to react with  $\alpha$ -Al<sub>2</sub>O<sub>3</sub> and additional O to form AlNbO<sub>4</sub>. The compositionally sharp interface in regions without grain boundaries shows that the Al<sub>2</sub>O<sub>3</sub>–Nb interface is, in principle, high-temperature stable. A larger Nb grain size is nevertheless essential to prevent interfacial oxide formation which supports the initially proposed approach toward coarse-grained ceramic refractory metal composites. The significantly increased O content in Nb<sub>bcc</sub> in the vicinity of Nb<sub>bcc</sub> grain boundaries indicates that more extensive heat treatment of the unprotected Nb film will eventually give rise to nucleation of Nb oxide throughout the entire film.

## 5. Experimental Section

Evochem (Evochem Advanced Materials GmbH, Offenbach, Germany) supplied <0001>-oriented sapphire substrates with dimensions of  $10 \times 10 \times 0.5$  mm in a polished state (roughness  $R_a < 0.3$  nm). The substrates were cleaned with acetone in an ultrasonic bath for 15 min. The samples were prepared by magnetron sputtering of Nb in a Leybold Z 550 sputter coater (sputtering target: 99.5 at% purity, Evochem

Advanced Materials GmbH, Offenbach, Germany, diameter 75 mm, thickness 5 mm) to achieve a film thickness of up to 30 µm Nb on the substrate. No plasma etching of the sapphire substrates was performed before deposition to avoid altering the local structure of planes terminating the  $\alpha$ -Al<sub>2</sub>O<sub>3</sub> surface. Prior to deposition, the target was sputter cleaned to remove possible surface contamination. Ar at 0.4 Pa and 500 W direct current power at the target were used for deposition on a nonheated substrate with a target–substrate distance of 50 mm.

A subsequent annealing treatment was done in a Setaram Setsys simultaneous thermal analysis (STA) device at 1600 °C for 2 h with heating and cooling rates of 10 K min<sup>-1</sup> under 6.0 Ar at 10<sup>5</sup> Pa, that is, an O partial pressure of 0.1 Pa (determined with a Zirox SGM5T ZrO<sub>2</sub> sensor) in the chamber before heating. The STA was equipped with a graphite heater, a graphite furnace chamber, and a tungsten measuring unit. During operation, the parts in the chamber made from graphite acted as O getters. The specimen was wrapped in a Nb foil (99.8 at%, Evochem) as an additional O getter and placed in a W crucible. The O<sub>2</sub> concentration in the chamber during operation was 10<sup>-20</sup> ppm according to the ZrO<sub>2</sub> sensor, which would correspond to a partial pressure of 10<sup>-21</sup> Pa, that is, negligible O supply from the Ar atmosphere. It should be noted that this value cannot be regarded as quantitative and only indicates the absence of technologically measurable O<sub>2</sub> species. X-ray diffraction was performed in a Malvern Panalytical Empyrean diffractometer with Cu K $\alpha$  radiation ( $\lambda = 1.5406$  Å, 40 kV, 40 mA) in Bragg–Brentano geometry. A step size of 0.0131° with 150 s per step was used with a PIXCEL3D Medipix3 1 × 1 detector in 1D line mode.

The samples were cut with a diamond wire saw, and APT tips and TEM lamellae were prepared by FIB milling from the cross section in a Zeiss Auriga 60 dual-beam SEM/FIB with conventional FIB procedures.<sup>[67,68]</sup> APT measurements were conducted using a Cameca LEAP 4000X HR in laser mode at a base temperature of 50 K, pulse frequency of 100 kHz, laser energy of 60 pJ, and target detection rate of 0.3%. Data reconstruction and analysis were performed in Cameca AP Suite 6.1. TEM including EDX was performed with a ThermoFisher Themis-Z double-corrected analytical (S)TEM operated at 300 kV and a Super-X EDX detector.

## Acknowledgements

The authors thank the German Research Foundation DFG for financial support through the research unit FOR3010 (project no. 416817512, HE 1872 40-1, and BO 5154 1-1). This work was partly carried out with the support of the Karlsruhe Nano Micro Facility (KNMFi, www.knmf.kit.edu), a Helmholtz Research Infrastructure at Karlsruhe Institute of Technology (KIT, www.kit.edu) (proposal 029755). Gratitude extends to Delphine Chassaing, who supported the work with focused ion beam specimen preparation. The research data is accessible in a KITopen repository. Open Access funding enabled and organized by Projekt DEAL.

## Conflict of Interest

The authors declare no conflict of interest.

## Data Availability Statement

The data that support the findings of this study are available from the corresponding author upon reasonable request.

## Keywords

grain boundary diffusion, high-resolution microscopy, interfacial oxide formation, nanocrystalline refractory metal–ceramic composites

Received: October 5, 2022

Revised: February 24, 2023

Published online:

- [1] V. D. Krstic, *Philos. Mag. A* **1983**, *48*, 695.
- [2] L. S. Sigl, P. A. Mataga, B. J. Dalgleish, R. M. McMeeking, A. G. Evans, *Acta Metall.* **1988**, *36*, 945.
- [3] D. E. García, S. Schicker, R. Janssen, N. Claussen, *J. Eur. Ceram. Soc.* **1998**, *18*, 601.
- [4] C. Scheu, G. Dehm, W. D. Kaplan, D. E. García, N. Claussen, *J. Am. Ceram. Soc.* **2000**, *83*, 397.
- [5] E. del Rio, J. M. Nash, J. C. Williams, M. C. Breslin, G. S. Daehn, *Mater. Sci. Eng. A* **2007**, *463*, 115.
- [6] T. Zienert, M. Farhani, S. Dudczig, C. G. Aneziris, *Ceram. Int.* **2018**, *44*, 16809.
- [7] G. Günay, T. Zienert, D. Endler, C. G. Aneziris, H. Biermann, A. Weidner, *Adv. Eng. Mater.* **2022**, *24*, 2200292.
- [8] B. Kraft, S. Wagner, K. G. Schell, M. J. Hoffmann, *Adv. Eng. Mater.* **2022**, *24*, 2200063.
- [9] K. Wang, R. R. Reeber, *Mater. Sci. Eng. R* **1998**, *23*, 101.
- [10] G. K. White, R. B. Roberts, *High Temp. Pressure* **1983**, *15*, 321.
- [11] T. Zienert, D. Endler, J. Hubálková, G. Günay, A. Weidner, H. Biermann, B. Kraft, S. Wagner, C. G. Aneziris, *Materials* **2021**, *14*, 6453.
- [12] T. Zienert, D. Endler, N. Brachhold, M. Weiner, M. Schmidtchen, U. Prah, C. G. Aneziris, *Adv. Eng. Mater.* **2022**, *24*, 2200407.
- [13] T. Zienert, D. Endler, J. Hubálková, P. Gehre, M. Eusterholz, T. Boll, M. Heilmaier, G. Günay, A. Weidner, H. Biermann, B. Kraft, S. Wagner, C. G. Aneziris, *Adv. Eng. Mater.* **2022**, *24*, 2200296.
- [14] A. Weidner, Y. Ranglack-Klemm, T. Zienert, C. G. Aneziris, H. Biermann, *Materials* **2019**, *12*, 3927.
- [15] M. K. Eusterholz, T. Boll, J. Gebauer, A. Weidner, A. Kauffmann, P. Franke, H. J. Seifert, H. Biermann, C. G. Aneziris, M. Heilmaier, *Adv. Eng. Mater.* **2022**, *24*, 2200161.
- [16] J. R. Donoso, R. E. Reed-Hill, *Metall. Trans. A* **1976**, *7*, 961.
- [17] P. J. Yang, Q. J. Li, T. Tsuru, S. Ogata, J. W. Zhang, H. W. Sheng, Z. W. Shan, G. Sha, W. Z. Han, J. Li, E. Ma, *Acta Mater.* **2019**, *168*, 331.
- [18] D. L. Douglass, *J. Less-Common Met.* **1963**, *5*, 151.
- [19] D. J. Larson, T. J. Prosa, R. M. Ulfig, B. P. Geiser, T. F. Kelly, *Local Electrode Atom Probe Tomography*, Springer Science+Business Media, New York, NY, USA **2013**, <https://doi.org/10.1007/978-1-4614-8721-0>.
- [20] T. F. Kelly, M. K. Miller, *Rev. Sci. Instrum.* **2007**, *78*, 031101.
- [21] E. A. Marquis, M. Bachhav, Y. Chen, Y. Dong, L. M. Gordon, A. McFarland, *Curr. Opin. Solid State Mater. Sci.* **2013**, *17*, 217.
- [22] *Atom Probe Tomography* (Eds: W. Lefebvre-Ulrikson, F. Vurpillot, X. Sauvage), Elsevier, London **2016**, <https://doi.org/10.1016/B978-0-12-804647-0.01001-9>.
- [23] M. C. Morris, H. F. McMurdie, E. H. Evans, B. Paretzkin, H. S. Parker, N. P. Pyrras, C. R. Hubbard, *Natl. Bur. Stand.* **1982**, *25*, 67.
- [24] W. Mader, *MRS Proc.* **1986**, *82*, 403.
- [25] M. Kuwabara, J. C. H. Spence, M. Rühle, *J. Mater. Res.* **1989**, *4*, 972.
- [26] H. D'Amour, D. Schiferl, W. Denner, H. Schulz, W. B. Holzapfel, *J. Appl. Phys.* **1978**, *49*, 4411.
- [27] D. Blavette, P. Duval, L. Letellier, M. Guttman, *Acta Mater.* **1996**, *44*, 4995.
- [28] A. Portavoce, I. Blum, K. Hoummada, D. Mangelinck, L. Chow, J. Bernardini, *Defect Diffus. Forum.* **2012**, *322*, 129.
- [29] S. Kölling, W. Vandervorst, *Ultramicroscopy* **2009**, *109*, 486.
- [30] D. W. Saxey, *Ultramicroscopy* **2011**, *111*, 473.



- [31] D. Santhanagopalan, D. K. Schreiber, D. E. Perea, R. L. Martens, Y. Janssen, P. Khalifah, Y. S. Meng, *Ultramicroscopy* **2015**, *148*, 57.
- [32] B. Gault, D. W. Saxey, M. W. Ashton, S. B. Sinnott, A. N. Chiamonti, M. P. Moody, D. K. Schreiber, *New J. Phys.* **2016**, *18*, 033031.
- [33] M. Karahka, Y. Xia, H. J. Kreuzer, *Appl. Phys. Lett.* **2015**, *107*, 2.
- [34] *Binary Alloy Phase Diagrams* (Eds: T.B. Massalski, H. Okamoto, P. Subramanian, L. Kacprzak, W.W. Scott), Vol. 2, Materials Information Soc., Materials Park (OH) **1986**, <https://doi.org/10.1002/adma.19910031215>.
- [35] B. W. Krakauer, D. N. Seidman, *Phys. Rev. B* **1993**, *48*, 6724.
- [36] J. W. Edwards, R. Speiser, H. L. Johnston, *J. Appl. Phys.* **1951**, *22*, 424.
- [37] M. E. Straumanis, S. Zyszczyński, *J. Appl. Crystallogr.* **1970**, *3*, 1.
- [38] J. A. Thornton, *Opt. Thin Film* **1988**, *821*, 95.
- [39] M. L. Kronberg, *Acta Metall.* **1957**, *5*, 507.
- [40] W. E. Lee, K. P. D. Lagerlof, *J. Electron Microsc. Tech.* **1985**, *2*, 247.
- [41] K. Burger, W. Mader, M. Rühle, *Ultramicroscopy* **1987**, *22*, 1.
- [42] W. Mader, M. Rühle, *Acta Metall.* **1989**, *37*, 853.
- [43] J. Mayer, J. A. Dura, C. P. Flynn, M. Rühle, *Surf. Coat. Technol.* **1990**, *43–44*, 199.
- [44] G. Gutekunst, J. Mayer, M. Rühle, *Philos. Mag. A* **1997**, *75*, 1329.
- [45] G. Gutekunst, J. Mayer, V. Vitek, M. Rühle, *Philos. Mag. A* **1997**, *75*, 1357.
- [46] J. Mayer, C. P. Flynn, *Ultramicroscopy* **1990**, *33*, 51.
- [47] J. Gebauer, P. Franke, H. J. Seifert, *Adv. Eng. Mater.* **2022**, *24*, 2200162.
- [48] M. X. Zhang, Y. A. Chang, *J. Phase Equilib.* **1994**, *15*, 470.
- [49] M. W. Chase, J. L. Curnutt, H. Prophet, R. A. McDonald, A. N. Syverud, *J. Phys. Chem. Ref. Data* **1975**, *4*, 1.
- [50] M. W. Chase, J. L. Curnutt, R. A. McDonald, A. N. Syverud, *J. Phys. Chem. Ref. Data* **1978**, *7*, 793.
- [51] B. Predel, *Li-Mg - Nd-Zr*, Vol. 5H, Springer-Verlag, Berlin Heidelberg **1997**, <https://doi.org/10.1007/b58857>.
- [52] A. L. Bowman, T. C. Wallace, J. L. Yarnell, R. G. Wenzel, *Acta Crystallogr.* **1966**, *21*, 843.
- [53] E. R. Pollard Jr., Electronic Properties of Niobium Monoxide, Doctoral dissertation, Massachusetts Institute of Technology **1968**.
- [54] C. Nico, T. Monteiro, M. P. F. Graça, *Prog. Mater. Sci.* **2016**, *80*, 1.
- [55] A. Taylor, N. J. Doyle, *J. Appl. Crystallogr.* **1971**, *4*, 103.
- [56] A. K. Cheetham, C. N. R. Rao, *Acta Crystallogr. Sect. B* **1976**, *32*, 1579.
- [57] D. S. Rimai, R. J. Sladek, *Phys. Rev. B* **1978**, *18*, 2807.
- [58] Y. Zhao, Z. Zhang, Y. Lin, *J. Phys. D: Appl. Phys.* **2004**, *37*, 3392.
- [59] R. F. Janninck, D. H. Whitmore, *J. Phys. Chem. Solids* **1966**, *27*, 1183.
- [60] K. Sakata, *J. Phys. Soc. Jpn.* **1969**, *26*, 582.
- [61] J. Wang, L. Chen, L. Zhang, C. Su, J. Feng, *Ceram. Int.* **2022**, *48*, 34697.
- [62] H. Jiang, M. Hirohasi, Y. Lu, H. Imanari, *Scr. Mater.* **2002**, *46*, 639.
- [63] Y. S. He, R. Hu, W. Z. Luo, T. He, X. H. Liu, *Rare Met.* **2018**, *37*, 838.
- [64] P. Tabero, *J. Therm. Anal. Calorim.* **2007**, *88*, 269.
- [65] M. R. N. Soares, S. Leite, C. Nico, M. Peres, A. J. S. Fernandes, M. P. F. Graça, M. Matos, R. Monteiro, T. Monteiro, F. M. Costa, *J. Eur. Ceram. Soc.* **2011**, *31*, 501.
- [66] V. Srikanth, E. C. Subbarao, G. V. Rao, *Ceram. Int.* **1992**, *18*, 251.
- [67] M. K. Miller, K. F. Russell, G. B. Thompson, *Ultramicroscopy* **2005**, *102*, 287.
- [68] J. M. Cairney, D. W. Saxey, D. McGrouther, S. P. Ringer, *Phys. B Condens. Matter.* **2007**, *394*, 267.